

Femtosecond pulsed laser deposited Er³⁺-doped zinc-sodium tellurite glass on Si: Thin-film structural and photoluminescence properties

Cite as: AIP Advances 9, 085324 (2019); <https://doi.org/10.1063/1.5097506>

Submitted: 26 March 2019 . Accepted: 21 August 2019 . Published Online: 28 August 2019

Thomas Mann , Billy Richards, Eric Kumi-Barimah , Robert Mathieson, Matthew Murray, Zoran Ikonc, Paul Steenson, Christopher Russell, and Gin Jose



View Online



Export Citation



CrossMark

ARTICLES YOU MAY BE INTERESTED IN

[A study on the surface morphology evolution of the GH4619 using warm laser shock peening](#)

AIP Advances 9, 085030 (2019); <https://doi.org/10.1063/1.5082755>

[Extreme brightness laser-based neutron pulses as a pathway for investigating nucleosynthesis in the laboratory](#)

Matter and Radiation at Extremes 4, 054402 (2019); <https://doi.org/10.1063/1.5081666>

[Rare earth-implanted lithium niobate: Properties and on-chip integration](#)

Applied Physics Letters 115, 071104 (2019); <https://doi.org/10.1063/1.5098316>



NEW

AVS Quantum Science

A high impact interdisciplinary journal for **ALL** quantum science

ACCEPTING SUBMISSIONS

Femtosecond pulsed laser deposited Er³⁺-doped zinc-sodium tellurite glass on Si: Thin-film structural and photoluminescence properties

Cite as: AIP Advances 9, 085324 (2019); doi: 10.1063/1.5097506

Submitted: 26 March 2019 • Accepted: 21 August 2019 •

Published Online: 28 August 2019



View Online



Export Citation



CrossMark

Thomas Mann,¹  Billy Richards,¹ Eric Kumi-Barimah,¹  Robert Mathieson,¹ Matthew Murray,¹ Zoran Ikonc,² Paul Steenson,² Christopher Russell,² and Gin Jose^{1,a)}

AFFILIATIONS

¹School of Chemical and Process Engineering, University of Leeds, Leeds LS2 9JT, UK

²School of Electronic and Electrical Engineering, University of Leeds, Leeds LS2 9JT, UK

^{a)}C.Jose@leeds.ac.uk

ABSTRACT

We characterise the thin-film structural properties and photoluminescence of femtosecond (40 fs, 800 nm) pulsed laser deposited Er³⁺-doped zinc-sodium tellurite glass on Si as a function of laser fluence. The laser fluence regime required for the formation of films composed of nanoparticles without droplets is found, the composition and crystallinity of the deposited material is reported and the photoluminescence of the films is characterised in dependence of film thickness.

© 2019 Author(s). All article content, except where otherwise noted, is licensed under a Creative Commons Attribution (CC BY) license (<http://creativecommons.org/licenses/by/4.0/>). <https://doi.org/10.1063/1.5097506>

I. INTRODUCTION

Tellurite glasses are particularly well suited as hosts for rare-earth (RE) ions due to their high rare-earth solubility and low phonon energy.^{1–4} In particular, the ⁴I_{13/2} → ⁴I_{15/2} transition of Er³⁺ ions is centred at 1.54 μm, which lies in the low loss C-band of silica and can therefore be exploited for telecommunications. As such, the fabrication of Er³⁺-doped tellurite-based glass thin films is of interest for optical applications including sensors, waveguide amplifiers and lasers.^{2,5}

Pulsed laser deposition (PLD) has proven to be a valid and efficient technique for the stoichiometric transfer of material from target to a film on a substrate, which is not possible with the growth of films from atomic species.⁶ Nanosecond (ns) PLD has been used by several research groups to form Er³⁺-doped tellurite thin films.^{7–10} However, micrometer sized droplet formation resulting from violent subsurface heating effects during vaporisation of the target and gas phase condensation of the large volume of ablated material by the high energy pulses is a characteristic of ns-PLD that limits the capability of this technique.^{11–13} Due to the non-thermal energy deposition and lower pulse energies required for femtosecond (fs)

laser ablation, the formation of droplets can be avoided providing that the laser fluence is not too high.^{12,14} The formation of nanoparticles in ns-PLD occurs during gas phase condensation of an atomised plasma plume confined in a pressurised atmosphere. This is significantly different in fs-PLD, where nanoparticle generation occurs in vacuum and is thought to be due to mechanical fragmentation of the highly pressurised fluid undergoing rapid quenching during the hydrodynamic expansion.^{14,15} The majority of fs-PLD fabricated nanostructured films result from the random stacking of nanoparticles (NPs), typically in the 10 - 60 nm range.^{13,14,16–18}

Er³⁺-doped zinc-sodium tellurite glass NPs have recently been incorporated into polymers for low-cost integrated optical amplifiers using the fs-PLD technique.¹⁹ Similarly, the ultrafast laser plasma doping (ULPD) technique ablates a rare-earth (RE) doped zinc-sodium tellurite target onto a heated silica based substrate such that the subsequent interfacial dissolution forms RE-doped hybrid tellurite-silica thin films.^{20–23}

The species (ions, nanoparticles and droplets) in the ablation plume are a direct consequence of the fs laser and target properties. The high energy ions and electrons (atomic species) typically only

make up a few percent of the total ablated matter.¹⁴ At a fixed fs laser wavelength, pulse width, spot size and repetition rate, the laser fluence relative to the target ablation threshold is the key parameter dictating the particle size distribution in the ablation plume.^{12,14} The ablation threshold of Er³⁺-doped zinc-sodium tellurite glass in atmosphere irradiated with a fs laser of pulse duration 100 fs and central wavelength of 800 nm has been characterised previously.²⁴ It was found that the single shot ablation threshold was 0.32 J/cm² and dropped to a multipulse value of 0.14 J/cm² at a spot size of 32 μm. A characterisation of the nanoparticles and droplets in the fs ablation plume for tellurite glass does not exist in the literature and is the purpose of this work.

Structural characterisation is achieved through scanning electron microscopy studies of vacuum depositions on silicon substrates at varying laser fluences. The composition of the depositions and the crystalline structure are studied with energy dispersive X-ray spectroscopy and grazing incidence X-ray diffraction, respectively. The effect of the target glass surface roughness on the laser ablation threshold was also investigated. The radiative spontaneous emission (SE) rate of the Er³⁺-doped films was measured using time-resolved photoluminescence (PL) spectroscopy and compared with a quantum-electrodynamical model for the average SE rate for ions inside multilayer dielectric structures. An increase in decay rate for very thin films is observed due to the electric field confinement within the film and an increase in the non-radiative recombination processes. The latter is due to a combination of Auger quenching and energy backtransfer, which are known to limit the efficiency of room temperature Er³⁺ ion doped/deposited silicon based light sources.^{25–28}

II. EXPERIMENTAL SETUP

A. Sample fabrication

Depositions were performed using an amplified solid-state Ti:sapphire laser (Wyvern 1000-10, KMLabs) producing an almost diffraction limited beam ($M^2 < 1.3$) at a central wavelength of 800 nm (~53 nm full width half maximum) and pulse duration of ~40 fs. The maximum pulse energy at a 1 kHz repetition rate was ~4 mJ. The linearly polarised beam exiting from the laser source was focused onto the target surface with a 56.5 cm focal length plano-convex lens at a 60° angle of incidence. The elliptical laser spot on the sample surface was measured prior to ablation and had an area of $A \approx 8.5 \times 10^{-5}$ cm² (Gaussian beam waists of ~82 and 33 μm). The laser energy was determined with a pyroelectric detector and energy meter (PE50-DIF-C and Starlite Energy Meter, Ophir), and controlled with a half-wave plate and beam splitting polariser to give pulse energies E_p ranging from 18 to 433 μJ. In this work we report the average fluence of the laser pulse, $F = E_p/A$. All experiments were carried out in a vacuum ($< 1 \times 10^{-4}$ Torr) and at room temperature (23°C).

The target was an Er³⁺-doped zinc-sodium tellurite glass of composition 79TeO₂-10ZnO-10Na₂O-1Er₂O₃ mol.% (1ErTZN). Fabrication and characterisation of the target glass has been presented in Ref. 24. The glass was wet polished with P1200 grit silicon carbide (SiC) sandpaper to the dimensions of ~30 × 30 × 3 mm. The resulting surface roughness $R_a \approx 108$ nm (measured on a 100 × 100 μm region). For investigations into the effect of target

surface quality on the ablation plume, the target glass was given an optical polish to $R_a \approx 5$ nm.

The substrate was a polished silicon wafer (P < 100 > B doped, resistivity of 1-20 ohm-cm, diced into 10 mm by 10 mm squares, $R_a < 0.3$ nm) placed parallel to and 40 mm above the target surface. Each substrate was cleaned for 5 minutes in an ultrasonic bath with acetone and then isopropanol prior to depositions. The Si substrate was rotated at 5 RPM around its centre to give a uniform deposition and each deposition constituted the application of 180k pulses per cm² to the target surface directly below the substrate. Specifically, the laser rastering involved scanning 180 lines at a speed of 10 mm/s over a length larger than the substrate (22 mm) and moving the target in 0.1 mm steps perpendicular to the laser raster axis after each line (18 mm length in total).

B. Characterisation

Characterisation of the deposited films was studied by using high resolution scanning electron microscopy (SEM, Hitachi SU8230). In order to determine the size distribution of the particles, several SEM images were processed using Fiji.^{29,30} Deposition thicknesses d were evaluated on cross-sections after snapping the substrate from the rear. Elemental identification of the depositions was performed using energy-dispersive X-ray spectroscopy (EDX) coupled to the SEM (80mm² X-Max detector, Oxford Instruments). Point measurements were taken at the centre of droplets to minimise the effect of surface geometry on the results (the analysis assumes a flat surface). The strongest peak signal in the spectra corresponding to the Si substrate was not included in the analysis. Sodium and zinc both exhibit their L emission lines very close to each other and could not be resolved in the spectra. As a result the relative ratio of Zn to Na are inaccurate and this also impacts the quantification of the weight % of other elements as the normalisation to 100% is not accurate. As a result of these limitations, the compositional results with the EDX technique are semi-quantitative.

The average surface roughness R_a and the root mean square roughness R_{RMS} were characterised via atomic force microscopy (AFM) operating in tapping mode (Innova Atomic Force Microscope, Bruker with a μmasch AFM probe of 8 nm nominal tip radius) and averaging over areas at least several times larger than the largest features. The data was analysed with the open source software Gwyddion.^{31,32}

The crystallinity of the 3.32 J/cm² deposition was studied by grazing incidence X-ray diffraction (GIXRD). This was preferred over the standard $\theta/2\theta$ XRD configuration to avoid the signal from the silicon substrate that would otherwise swamp the spectral features of the thin film. GIXRD measurements were performed on an X-ray diffractometer (X'Pert, Phillips) using Cu-K α radiation (1.5406 Å) across the 2θ range 10 - 80° at an angle of incidence of 2° and a scan rate of 0.005°/second. The peaks in the measured diffraction patterns were identified and indexed using the X'pert High Score Plus software package. The spectral shift in the GXID spectra was -0.29° and evaluated prior to fitting using a $\theta/2\theta$ XRD scan on the same sample.³³

PL measurements were performed using a fluorescence spectrometer (FLS 920, Edinburgh Instruments) at room temperature. A 976 nm excitation laser source (BL976-PAG500976, Thorlabs), which resonates with the $^4I_{15/2} \rightarrow ^4I_{11/2}$ transition of Er³⁺, with a

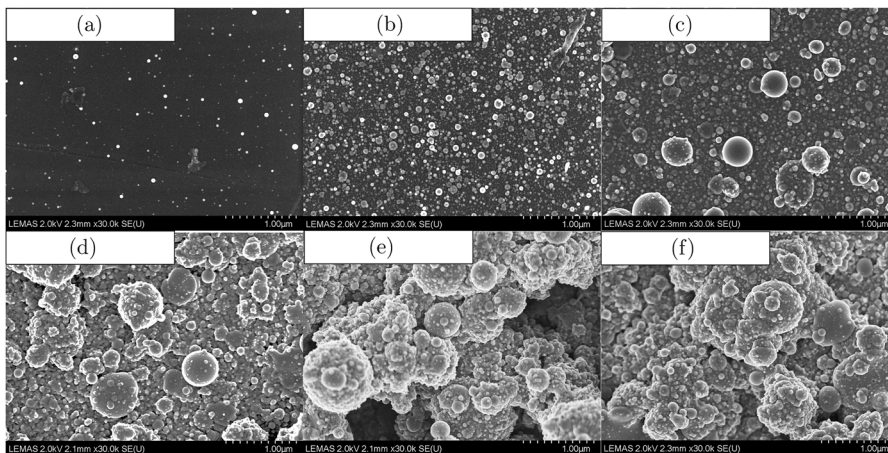


FIG. 1. SEM images of depositions at a spot size of $A = 8.57 \times 10^{-5} \text{ cm}^2$ and varying laser fluences; (a) $F = 0.20 \text{ J/cm}^2$, (b) $F = 0.73 \text{ J/cm}^2$, (c) $F = 1.25 \text{ J/cm}^2$, (d) $F = 2.05 \text{ J/cm}^2$, (e) $F = 3.32 \text{ J/cm}^2$, (f) $F = 5.31 \text{ J/cm}^2$.

power of 375 mW was focused to a spot size of approximately 1 mm at an angle of 45° to the sample normal (the target was excited on the edge at 0° to avoid radiation trapping effects). The $1.54 \mu\text{m}$ centred PL band, corresponding to the $^4I_{13/2} \rightarrow ^4I_{15/2}$ transition of Er^{3+} was also collected at 45° (90° for the target) and initially spectrally analysed with a single grating monochromator, detected with a liquid-nitrogen cooled photomultiplier tube (Hamamatsu) and then analysed with a photon counting multichannel scaler (PMS-400A, Becker and Hickl) with an overall time resolution of $10 \mu\text{s}$. The steady state emission PL spectra of the samples were acquired in 0.5 nm steps from 1400 to 1700 nm with a 0.2 s dwell time. For the time-resolved PL measurement a 0.1 ms excitation pulse, modulated electronically at a frequency of 10 Hz, was accumulated over 400 sweeps and fitted with a single exponential curve. Due to the reduced signal to noise ratio of the two lowest fluence depositions, a pump time of 5 ms (to steady state) was used to maximise the signal and 2000 sweeps were collected. The fits to the decays all had a chi-squared value of less than 1.1 and flat residuals indicating a good fit.

III. RESULTS AND DISCUSSION

A. Physical and structural properties

SEM images for depositions at six fluences increasing from close to the predicted ablation threshold (the multipulse value $F_{\text{th}}(\infty) = 0.14 \text{ J/cm}^2$)²⁴ are shown in Fig. 1. It is apparent that with increasing fluence, the deposition rate increases along with the particle size. At the lowest fluence of 0.2 J/cm^2 , the particles are in the nanometer size range and well dispersed with an area coverage on the substrate of only $\sim 1.65\%$. The size distribution of the NPs is shown in Fig. 2 and followed a log-normal distribution with an average radius of 12 nm and a standard deviation of 8.6 nm. No nanoparticles had a radius of more than 65 nm.

For ablations at and above 1.25 J/cm^2 , Fig. 1 shows the presence of a second distribution of much larger particles, known as droplets, that increase in size with laser fluence. Estimates of the maximum sizes of the droplets from the SEM images are presented in Fig. 3 and quickly reach micron size even at a relatively low fluence of 1 J/cm^2 . The surface roughness, given in Table 1, increases in an

exponential manner with laser fluence and was too rough to measure at the highest deposition fluence.

Comparing Fig. 4 with the cross-sections in Fig. 1 it is clear that the films are formed through the random stacking of NPs and droplets, as is typical for fs-PLD.¹⁷ The thickness of the films showed an exponential increase with laser fluence, as given in Table I and

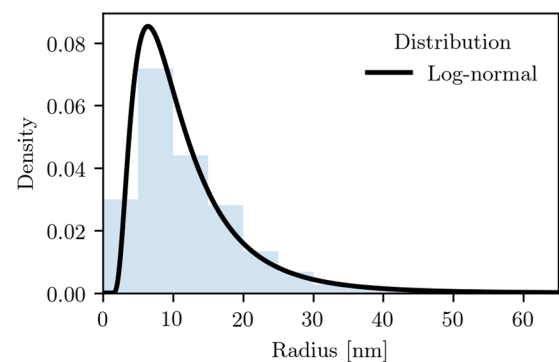


FIG. 2. Particle size distribution for a deposition at 0.2 J/cm^2 . Bin sizes were 5 nm. The fitted log-normal distribution (black line) had an average radius of 12 nm and a standard deviation of 8.6 nm.

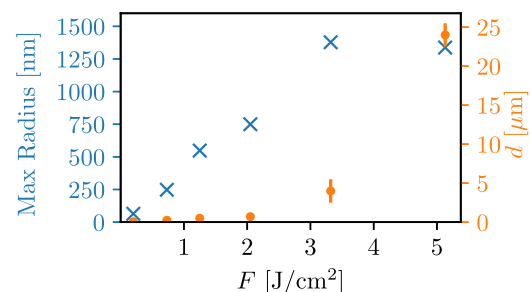


FIG. 3. The maximum particle sizes (marked with x) and corresponding film thickness (marked with circles) against laser fluence. Values are measured from SEM images of several locations on the sample.

TABLE I. Physical and photoluminescence properties of depositions at varying laser fluences. d is the thickness, τ is the photoluminescence lifetime and FWHM is the full width at half maximum of the photoluminescence spectra.

F [J/cm ²]	d [nm]	R_a [nm]	R_{RMS} [nm]	τ [ms]	FWHM [nm]
0.20	20 ± 20	7.5	12.5	2.35 ± 0.08	–
0.73	240 ± 150	13.8	18.1	2.69 ± 0.03	–
1.25	500 ± 200	81.5	123.5	3.49 ± 0.03	37.8
2.05	700 ± 250	226.9	308.8	3.50 ± 0.01	37.4
3.32	4000 ± 1500	577.3	700.0	3.45 ± 0.01	38.7
5.13	24000 ± 1500	–	–	3.36 ± 0.05	37.4

Fig. 3, which is a due to the exponential dependence in ablated volume with fluence.²⁴

The composition of the target glass and the depositions are reported in Table II. The average composition of the depositions in at.% was 17 Te, 68 O, 4.5 Zn, 9.5 Na and 1.1 Er. The reduced tellurium content of the depositions compared to the target of ~9% is attributed to the fact that the most volatile element (heat of vaporization, 52.55 kJ/mol) in the ablated species, namely tellurium, preferentially evaporates off during early transport in the plume.¹⁷ The reduction in tellurium was responsible for the increase in concentration of all other elements (note that the total concentration of Zn and Na must be compared). The small variations in composition with laser fluence were not significant enough for any further conclusions to be made from the semi-quantitative EDX data. The Er³⁺-doping concentration, assuming the density of the target $\rho_{\text{ErTZN}} = 5.24 \text{ g/cm}^3$,²⁴ was $8.78 \times 10^{20} \text{ cm}^{-3}$. This is 3.4 times higher than in the target which had a Er³⁺-doping concentration of $2.58 \times 10^{20} \text{ cm}^{-3}$. Changes in composition between the NPs and droplets may be possible due to the different formation processes in the plume but

can not be measured with EDX due to the small spatial resolution required.

The GIXRD pattern of the film deposited at a laser fluence of 3.32 J/cm² is presented in Fig. 5. The peak of the Si(100) substrate at $2\theta = 69.8^\circ$ is not observed, confirming that all peaks are from the deposited material. The diffraction peaks indicate that the material exhibits crystalline phases and is not amorphous like the target. Finding an exact match to the broad overlapping peaks of the multiple crystalline phases with the existing ICDD database was not possible and so the approach used here was to identify the known crystal structures and compare them to the measured GIXRD pattern.³⁴ The spectra is dominated by peaks centred at $2\theta = 26.28^\circ$ and 26.58° . The broad nature of the high intensity spike indicates the presence of additional peaks, however these could not be spectrally resolved. The peaks were indexed to tellurium oxide (γ -TeO₂ (101) and (120), ICDD reference code: 04-014-3924) and zinc tellurium oxide (Zn₂Te₃O₈ (-311)/(310), ICDD reference code: 04-012-2189). All other peaks were much smaller with a relative intensity of <4%. A sharp peak with the next highest intensity at $2\theta = 56.80^\circ$ corresponded to Zn₂Te₃O₈ (-331)/(-117). The rest of the spectra contained broad and weak peaks corresponding to multiple crystalline planes. The broad peaks at 18.10° , 38.15° , 44.43° , 54.77° and 56.80° were indexed to Zn₂Te₃O₈, while the peaks at 54.14° and 55.94° were indexed to γ -TeO₂. The remaining peaks at 29.09° , 36.66° , 42.70° , 59.65° , 76.91° , 77.38° and 77.83° resulted from combinations of the various crystalline planes of Zn₂Te₃O₈ and γ -TeO₂. Tellurium was present in both the crystalline structures due to it being the highest concentration element in the deposited material.

A comparison with previous research shows that the formation of crystalline phases in ultrafast laser depositions of tellurite glass is not surprising. Kumi-Barimah *et al.*¹⁹ observed crystallisation for NPs implanted in polymer heated at 373 K (100°C) from the selected area electron diffraction (SAED) patterns, however they

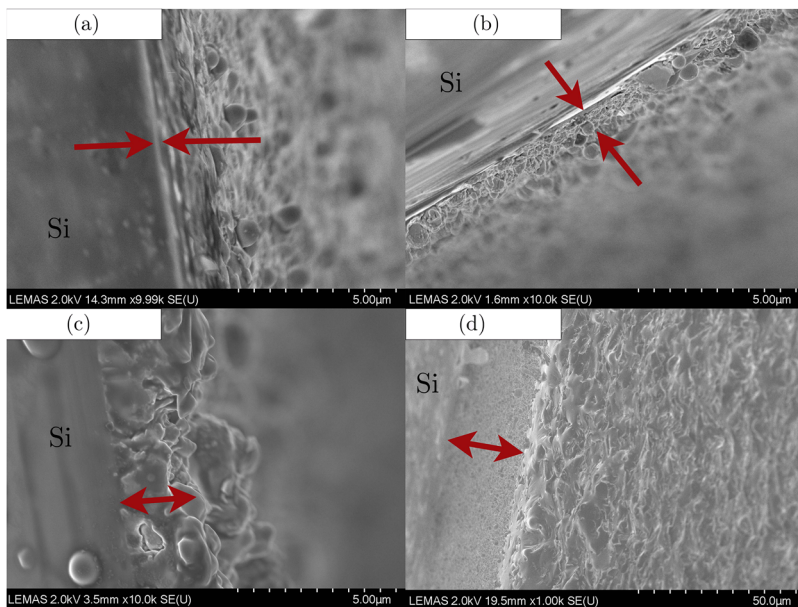


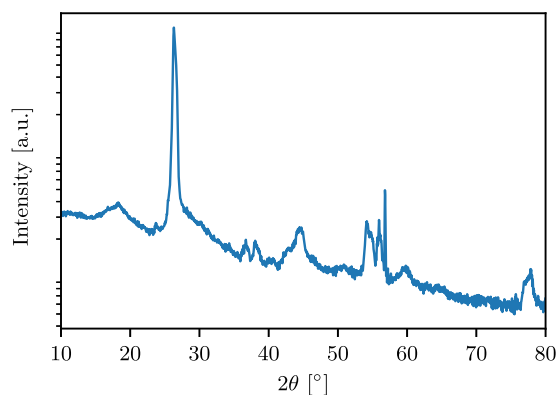
FIG. 4. Cross section SEM images of depositions at a spot size of $A = 8.6 \times 10^{-5} \text{ cm}^2$ and varying laser fluences; (a) $F = 1.25 \text{ J/cm}^2$, (b) $F = 2.05 \text{ J/cm}^2$, (c) $F = 3.32 \text{ J/cm}^2$ and (d) 5.13 J/cm^2 . Note that (d) has a different scale bar to the other images. The Si substrate is indicated with text and the depositions with arrows.

TABLE II. The atomic composition of the 1ErTZN target glass and the depositions at different laser fluences.

	Element [at. %]				
	Te	O	Zn	Na	Er
Target 1ErTZN ^a	26.3	61.6	5.0	6.7	0.4
	F [J/cm ²]				
1.25	17.0	66.1	5.3	10.5	1.1
2.05	16.4	69.6	4.3	8.7	1.0
3.32	17.6	69.1	3.8	8.5	1.0
5.13	17.2	67.1	4.5	10.1	1.1

^aCalculated from the molecular formula of the target glass. The evaporation of Te during melting is not taken into account.

were unable to identify the crystals as no peaks were observed in the XRD patterns. This was likely due to the fact that the polymer substrate had a large background signal as the GIXRD method was not used. SAED patterns in room temperature deposited films on silica have also shown unidentified crystalline phases.³⁵ The crystalline phases identified in this research explain the observations in both these works, as the experimental conditions are similar. We also note that the substrate temperature during deposition on silica plays a key role on the film crystallisation. XRD analysis of films fabricated at 673 K (400° C) on silica-on-silicon has shown the presence of Zn₂Te₃O₈ with miller indices of (111) and (332) and Na₂TeO₃ with miller indices of (022) and (242) crystals.³⁶ However, for higher temperatures of 843 K (≈570°), dissolution between the deposited target and the substrate glasses forming a hybrid layer resulted in amorphous films.^{21,36} The term ‘ultrafast laser plasma doping’ is used for amorphous hybrid films fabricated in this temperature regime and using this technique.^{20–23,35–37} The progressive formation of TeO₂, ZnO, Na₂Si₂O₅ and SiO₂ crystalline structures during annealing above 923 K (650° C) has also been shown using XRD studies of amorphous hybrid tellurite-silica films by Chandrappan *et al.*³⁷

**FIG. 5.** Grazing incidence X-ray diffraction patterns of a deposition at $F = 3.32$ J/cm² on a logarithmic scale. The peaks are identified in the text.

The NPs and droplets have a similar composition to the target glass, which has a melting temperature $T_m \approx 850$ K (measured for 75TeO₂-20ZnO-2.25Na₂O-2.25Li₂O-0.5NaF (mol%) glass³⁸), crystallisation temperature $T_x = 694$ K and transition temperature $T_g = 565$ K (measured for 80TeO₂-10ZnO-10Na₂O (mol%) glass³⁹). Initial NP temperatures (1 mm distance from the target) depend on the critical point and are typically of the order ≈ 2000 K for gold and silicon.⁴⁰ Assuming a similar heating regime, the NPs and droplets have a temperature $T > T_m$ and are in a molten state. Amoruso *et al.*⁴¹ have shown that radiative cooling dominates during late stage plume expansion and occurs at rates of 28 K/ μ s, 6.5 K/ μ s and 0.9 K/ μ s for NPs at T of 2000 K, 1500 K and 1000 K, respectively. Impact and deposition on the substrate with a temperature $< T_x$ will result in a much more rapid quenching that would not favour crystallisation. The formation of crystalline phases must therefore occur during plume transport and depends on the speed of the species and the target-substrate distance. This conclusion is supported by the previously mentioned research that has found crystalline films for all substrate temperatures that are not $\gg T_x$, (i.e. outside the ultrafast laser plasma doping regime). Boulmer-Leborgne *et al.*¹³ found that NPs travelled at a few 10⁴ cm/s while droplets travelled with slightly slower velocities of several 10³ cm/s, regardless of the ablated material (metal, semiconductor and insulator). As a result the droplets undergo longer periods of radiative cooling and are deposited in a colder and less compliant state. This is seen in Fig. 4(a) and (b) where the droplets have a highly spherical shape compared to the hemispherical NPs. We hypothesise that the fast NPs arrive at the substrate with $T > T_x$ and so are deposited in an amorphous state while the slower droplets have crystallised and cooled sufficiently to $T < T_x$ before deposition. This raises the possibility of forming amorphous tellurite films through the use of low laser fluences to eliminate the presence of droplets.

B. Target surface quality

SEM images comparing a deposition at $F = 1.67$ J/cm² using an optically polished target of $R_a \approx 5$ nm with depositions at $F = 0.20$ and 0.73 J/cm² using a rough target of $R_a \approx 108$ nm (as characterised in Section III A) are shown in Fig. 6. The volume of material ablated using an optically polished target is much lower than that of a rough target. Surface roughness can trap light and enhances near-field effects leading to an improved light-matter coupling and hence a reduction in ablation threshold. A second clear observation is the increased fraction of droplets to NP in the ablated matter. This is an important consideration for fs-PLD type applications and, as far as we are aware, this effect has not been reported in the literature.

We have previously reported that the change in ablation threshold in atmosphere of a tellurite glass that is optically polished to one that has had numerous incubating pulses, which cause roughening, is $F_{th}(1)/F_{th}(\infty) = 0.32/0.14 = 2.29$.²⁴ Additionally, Ben-Yakar and Byer⁴² observed that for borosilicate glass the change in single pulse ablation threshold $F_{th}(1)$ from vacuum ($< 7.5 \times 10^{-5}$ Torr) to air was $4.1/2.6 = 1.58 \approx 1.6$ and the corresponding multipulse $F_{th}(\infty)$ change was $1.68/1.74 = 0.97 \approx 1$. The effect of reduced ablation threshold in atmosphere is attributed to an increase in the efficiency of plasma-surface coupling (i.e. heating) due to a decreased plume expansion.^{42–44} It may therefore be expected that the increase in ablation threshold of the optically polished compared to the rough

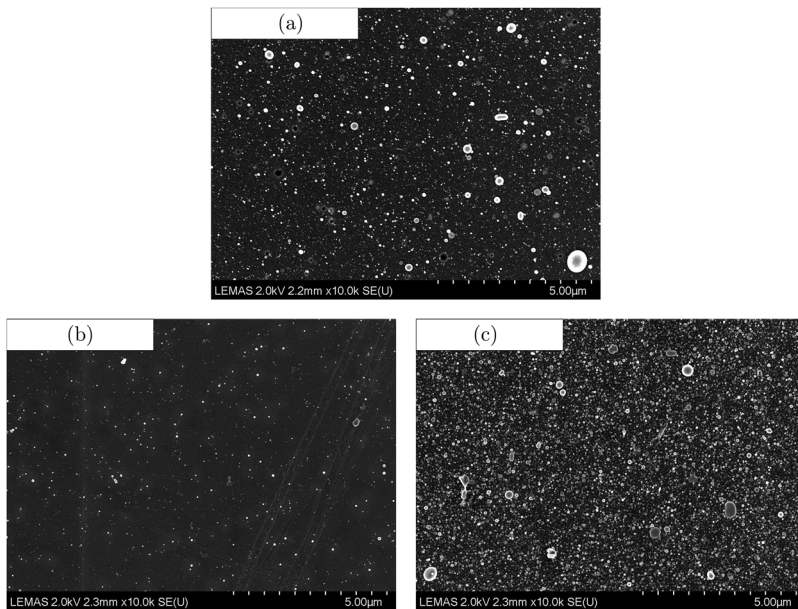


FIG. 6. Depositions at different laser fluences F using a target glass polished to (a) $R_a \approx 5$ nm and (b, c) $R_a \approx 108$ nm. (a) 1.67 J/cm². (b) 0.20 J/cm². (c) 0.73 J/cm².

polished tellurite glass in vacuum is $2.29 \times 1.6 \approx 3.7$. Hence, the $F = 1.67$ J/cm² in Fig. 6(a) should give a similar deposition using a rough polished target using $F \approx 0.45$ J/cm². This agrees well with a visual comparison of Fig. 6(b) and (c).

We conclude that for fs-PLD type applications the higher surface roughness is not only beneficial in terms of having a smaller particle size but also results in a reduced laser energy requirement. In addition to this, the damage that typically occurs to the surface during ablation typically results in a rough surface and should therefore be maintained from the very start of the deposition by using an unpolished target. The increased droplet fraction from smooth surfaces are also relevant for the more unique cases involving the ablation of liquids and requires more fundamental research to explain this phenomenon.

C. Optical properties

The PL spectra of the 1ErTZN target glass and depositions are shown in Fig. 7(a). It was not possible to characterise the PL spectra for the depositions at $F = 0.20$ J/cm² and 0.73 J/cm² as the PL emission was too weak due to the small volume of deposited material and low quantum efficiency (discussed later in this section). The spectra of all the depositions were almost identical, showing a Stark broadened peak centred at 1533 nm, like the target glass. There were no sharp spectral lines in the PL spectra, confirming that the optically active Er³⁺ ions remain in amorphous tellurite host. This is expected as the crystalline structures measured via GIXRD in Section III A do not correspond to crystalline phases of erbium. The full width at half maximum (FWHM) of the target was 68.0 nm and the FWHM of the depositions, reported in Table I, had an average of 37.8 ± 0.6 nm. Tellurite glass is known to exhibit broadened Er³⁺ ion fluorescence band and so the narrower FWHM of the deposition is a result of the decrease in Te concentration that was measured with EDX in Table II. The reduction in tellurium concentration also resulted in lower sidebands at 1503, 1555 and 1597 nm. The shoulder

at 1503 nm decreased in relative intensity from 0.43 to 0.39 with an increase in laser fluence of 1.25 J/cm² to 5.13 J/cm², which may be due to increased evaporation of Te during plume transport caused by the higher heating of the material by the laser.

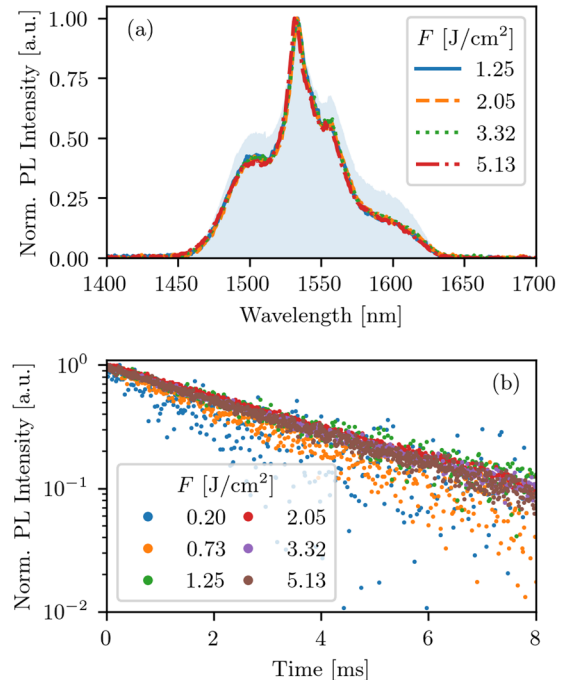


FIG. 7. Normalised photoluminescence (a) spectra and (b) decay of the particulate depositions at varying fluences. Shaded fill plot in (a) shows the spectra of the 1ErTZN target glass for reference.

The PL lifetime τ centred at $1.54 \mu\text{m}$ of the depositions were all shorter than the $4.34 \pm 0.02 \text{ ms}$ of the target, as shown in Fig. 7(b) and presented in Table I. For depositions at $F \geq 1.25 \text{ J/cm}^2$ where the average film thickness d was greater than $\sim 500 \text{ nm}$, τ was $3.45 \pm 0.07 \text{ ms}$. The decrease in lifetime from the target to the deposited films is due to the increased erbium concentration (see Table II) giving rise to more efficient concentration quenching.⁴⁵ For lower fluence depositions, where d was smaller, τ continued to decrease. The shortest lifetime measured was 69% of the films with $d \geq 500 \text{ nm}$ or $F \geq 1.25 \text{ J/cm}^2$. NPs implanted in polymers generated through fs laser ablation of Er^{3+} -doped TZN glass in a 70 mTorr oxygen atmosphere with $F \approx 1 \text{ J/cm}^2$ (spot size is estimated) exhibited identical spectra with a FWHM of 39.2 nm and a similar lifetime of $\tau \approx 4 \text{ ms}$.¹⁹ The role of low pressure oxygen background is therefore not important in determining the PL of ablated material. This may be expected at such low pressures as collisions of the plume species with the background gas atoms is almost negligible.^{43,46}

A decrease in PL lifetime with a decrease in laser fluence was observed for $F < 1.25 \text{ J/cm}^2$. As all the lifetimes were mono-exponential it may be expected that the compositional differences between the NPs and the droplets are small. The decrease in lifetime can therefore not be attributed solely to the lack of droplets for these low fluence depositions. Furthermore, the similarity in the PL spectra confirms this conclusion. The difference in τ is attributed to the film thickness as explained in the remainder of this section.

The decay rate $\Gamma = 1/\tau$ of an ion is composed of a radiative decay rate Γ_{rad} and a non-radiative decay rate Γ_{nrad} by

$$\Gamma = \Gamma_{\text{rad}} + \Gamma_{\text{nrad}}, \quad (1)$$

where the non-radiative decay rate is composed of the internal non-radiative recombination rate Γ_{int} and the concentration quenching rate due to ion-ion interactions Γ_{q} by $\Gamma_{\text{nrad}} = \Gamma_{\text{int}} + \Gamma_{\text{q}}$.

The spontaneous emission (SE) rate Γ_{rad} of a dipole is given by Fermi's golden rule and is proportional to the refractive index in a homogeneous dielectric media.^{47–49} Inside stratified dielectric media, electric field confinement effects due to the index contrast at the interfaces results in a position dependent $\Gamma_{\text{rad}}(z)$, where z is the position of the dipole in the axis perpendicular to the interfaces.⁵⁰ These effects become particularly important for thin films where all dipoles are close to interfaces as the experimentally measured Γ_{rad} represents an ensemble average of dipoles at all positions within the film. To investigate this effect, simulations were performed using a quantum-electrodynamical formalism suited to the analysis of the radiative SE rate in multilayer dielectric structures derived by Creatore and Andreani.⁵⁰ The multilayer dielectric structures consisted of a variable thickness d Er^{3+} -doped TZN layer (approximated to be the same as the 1ErTZN target $n_{1\text{ErTZN}} = 2.048^{24}$) bounded by an infinite Si ($n_{\text{Si}}=3.48$) substrate ($z \rightarrow -\infty$) and air ($n_{\text{air}}=1$) superstrate ($z \rightarrow \infty$) layers. The structures did not support emission into waveguiding modes as the Si substrate had the highest index. The radiative SE rates normalised to the free space value (Purcell factor, F_p) for a dipole emitting at $\lambda = 1.54 \mu\text{m}$ as a function of position for two multilayer structures with a d equal to 50 nm and 1540 nm is shown in Fig. 8. The decay rates for dipoles orientated perpendicular \perp , parallel \parallel and randomly $\text{Avg} = (2/3)\parallel + (1/3)\perp$ are shown. For Er^{3+} ions the randomly orientated dipole decay rate is relevant.

Dipoles in the thinner $d = 50 \text{ nm}$ film have an enhanced decay rate at most positions within the film originating from the parallel

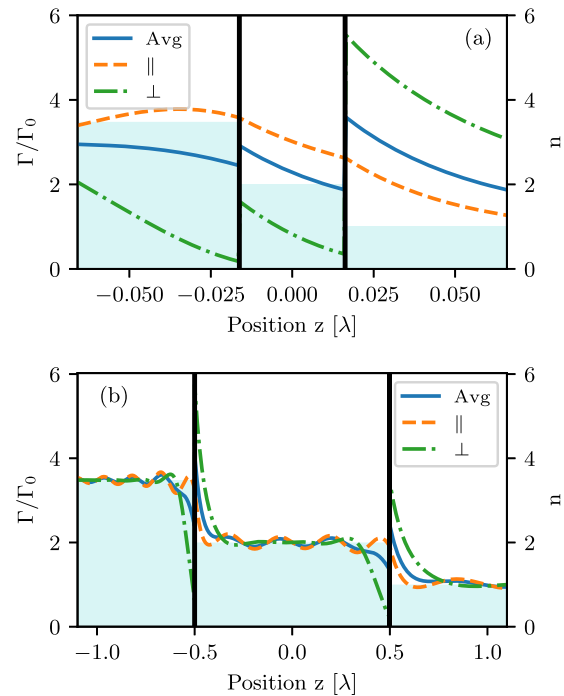


FIG. 8. The radiative decay rate of perpendicular \perp , parallel \parallel and randomly $\text{Avg} = (2/3)\parallel + (1/3)\perp$ orientated dipole compared to the free space decay rate at $\lambda = 1540 \text{ nm}$ as a function of position in a multilayer structure; Si substrate is at $z \rightarrow -\infty$, (a) 50 nm or (b) 1540 nm thick tellurite film, air superstrate is at $z \rightarrow -\infty$. The vertical black lines indicate the layer boundaries and the shaded light blue regions indicate the refractive index of the layer.

component that couples to TE modes. For the thicker $d = 1540 \text{ nm}$ film, the SE rate of randomly orientated dipoles is enhanced at the Si/ErTZN interface and suppressed at the air/ErTZN interface. For the majority of dipole positions in the film, which are far from the interfaces, the SE rate is unaffected by the interfaces and equals what would be measured in a bulk medium. The SE rate for dipoles located deep in the substrate/superstrate and far from the interfaces, the Purcell factor tends to the dielectric index as expected.^{47–49}

The theoretical average decay rate for randomly orientated dipoles averaged over all positions within a film, corresponding to the experimentally measured τ , for d ranging from 5 to 4000 nm is plotted alongside the experimental data in Fig. 9 (supplementary material shows an animation of the average SE rate as a function of position within the film for the different thicknesses). The theoretical and experimental trends are similar in that τ tends to the bulk value after a film thickness of $\sim 500 \text{ nm}$. This is in agreement with the experimental measurements of Er^{3+} ions implanted in sodalime silicate glass showing that films thicker than $1 \mu\text{m}$ had an average lifetime close to that of a bulk system.⁵¹ It is not expected for the experimental measurements to show the oscillations seen in the simulations as the surface roughness of the films results in a poorly defined film thickness. For thin films the experimentally measured τ drops like the theoretical predictions, however the decrease is greater for the experimental results.

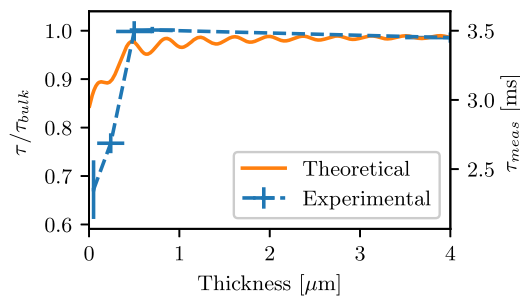


FIG. 9. Lifetime measured from the NP depositions at varying fluences compared to theoretical simulation of the average dipole decay rate within the film. Left scale shows the lifetime normalised to the bulk value (Purcell factor), which for experimental measurements is chosen to be 3.45 ms and theoretical calculations is $(1/n_{\text{bulk}})$ ms. Right scale shows the measured lifetime of the depositions. The 1ErTZN target had a lifetime of 4.34 ms.

For Er^{3+} ion implanted silicates doped to a similar concentration of $2 \times 10^{20} \text{ cm}^{-3}$, in which no clustering occurs, it has been shown that 100% of the Er^{3+} ions are in optically active states (i.e. 100% quantum efficiency).⁴⁵ Furthermore, the low phonon energy of tellurite glass ensures that internal non-radiative recombination of Er^{3+} ions from the first excited state does not occur through multiphonon emission.⁵² It is therefore assumed that $\Gamma_{\text{int}} = 0$ in this case. The Er^{3+} ions are assumed to always be within the same tellurite dielectric material and so local field effects are not considered.⁵³

At high doping concentrations energy migration, due to non-radiative short-range Förster energy transfer between ions, becomes more efficient and each transfer increases the probability that an ion coupled to a quenching centre is met. This non-radiative decay rate is characterised by Γ_q .⁴⁵ For Er^{3+} -doped silica glasses, OH-groups are known to be resonant quenching centres.⁵⁴ In this case, non-radiative decay processes are enhanced for ions close to the Si interface due to energy backtransfer and Auger quenching with free and bound charge carriers in silicon.²⁸ These effects are known to be significant in silica deposited slot waveguides on silicon, where an increased fraction of Er^{3+} ions are close to Si interfaces and limits both the possible gain of the structure and maximum Purcell factor enhancement possible.^{28,55} Energy migration effectively couples ions further from the interface to the Si quenching centres. As the films get thicker, increasing numbers of ion transfer processes are required to reach the Si quenching centres for the furthest ions and so the probability of non-radiative decay decreases. Thus for PL measurements of thicker films, where a greater fraction of Er^{3+} ions are far from the Si interface, the probability of non-radiative recombination through energy migration becomes negligible and so the average decay rate from the ensemble of ions $\Gamma = \Gamma_{\text{rad}}$. The radiative quantum efficiency $\Gamma_{\text{rad}}/(\Gamma_{\text{rad}} + \Gamma_{\text{nrad}}) = \Gamma_{\text{rad}}/\Gamma_{\text{meas}}$ for the thinnest 20 nm film (actually composed of disperse NPs) is 80% and so radiative recombination is still the dominant process. This value is larger than the 67% quantum efficiency measured for a reactive cosputtered 20 nm Er^{3+} -doped SiO_2 layer on Si (concentration $7.6 \times 10^{19} \text{ cm}^{-3}$). The difference is attributed to a combination of doping concentration and increase in thickness.

IV. CONCLUSION

Er^{3+} -doped zinc-sodium tellurite glass films formed through the random stacking of nanoparticles and droplets were deposited on Si in a vacuum at varying femtosecond laser fluences. For $F < 1.25 \text{ J/cm}^2$ the films were solely composed of nanoparticles with an average radius of 12 nm. The film thicknesses ranged from 20 nm to 24 μm at $F = 0.20 \text{ J/cm}^2$ and 5.13 J/cm^2 , respectively. The surface roughness of the films increased with laser fluence due to the droplets in the ablation plume. The depositions had tellurium oxide and zinc tellurium oxide crystalline phases that either formed by thermal quenching during the hydrodynamic expansion and plume transport or upon impact with the cool substrate. There was a slight $\sim 9\%$ loss in Te content during plume transport due to evaporation, which resulted in the increase in Er^{3+} concentration. The lifetime of the deposited films was reduced compared to the target as a result of the compositional changes. For films below $\sim 500 \text{ nm}$, the increase in the local density of states combined with an increase in the non-radiative recombination rate due to Auger quenching and energy backtransfer to Si resulted in shorter photoluminescence lifetimes and a reduction in quantum efficiency up to 80%.

The characterisation presented here for producing optically active tellurite-based glass NPs and thin films is directly applicable for optical devices and is also fundamental to the understanding of the ultrafast laser plasma doping technique. Furthermore, it has been shown that the femtosecond laser ablation threshold of tellurite glass does not vary for typical doping concentrations as the material linear absorption is not relevant in the highly non-linear process.²⁴ Doping the target glass with rare-earth elements other than erbium is trivial and, as such, films or NPs can be produced that have a wide range fluorescent bands, providing suitable rare-earth ion transitions exists, using these results.

SUPPLEMENTARY MATERIAL

See [supplementary material](#) for an animation of the simulated average SE rate of Er^{3+} ions as a function of position within tellurite deposited films on Si for different film thicknesses.

ACKNOWLEDGMENTS

We would like to thank Mr. Stuart Micklethwaite and Mr. John Harrington, Leeds Electron Microscopy and Spectroscopy (LEMAS) Centre, for support in carrying out the SEM measurements. This work was supported by the Engineering and Physical Sciences Research Council (EPSRC) (DTP Award reference No. 1559338) and all authors acknowledge the support of EPSRC project Nos. EP/M015165/1 and EP/M022854/1.

REFERENCES

- V. A. G. Rivera, D. Manzani, and V. A. G. Rivera, *Technological Advances in Tellurite Glasses* (Springer, 2017).
- S. Shen, A. Jha, X. Liu, M. Naftaly, K. Bindra, H. J. Bookey, and A. K. Kar, "Tellurite glasses for broadband amplifiers and integrated optics," *Journal of the American Ceramic Society* **85**, 1391–1395 (2002).
- A. Jha, B. D. O. Richards, G. Jose, T. Toney Fernandez, C. J. Hill, J. Lousteau, and P. Joshi, "Review on structural, thermal, optical and spectroscopic properties of tellurium oxide based glasses for fibre optic and waveguide applications," *International Materials Reviews* **57**, 357–382 (2012).

- ⁴W. J. Miniscalco, "Erbium-doped glasses for fiber amplifiers at 1500 nm," *Journal of Lightwave Technology* **9**, 234–250 (1991).
- ⁵P. Nandi, G. Jose, C. Jayakrishnan, S. Debbarma, K. Chalapathi, K. Alti, A. K. Dharmadhikari, J. A. Dharmadhikari, and D. Mathur, "Femtosecond laser written channel waveguides in tellurite glass," *Optics Express* **14**, 12145–12150 (2006).
- ⁶J. Schou, "Physical aspects of the pulsed laser deposition technique: The stoichiometric transfer of material from target to film," *Applied Surface Science* **255**, 5191–5198 (2009).
- ⁷D. H. Lowndes, C. M. Rouleau, T. Thundat, G. Duscher, E. A. Kenik, and S. J. Pennycook, "Silicon and zinc telluride nanoparticles synthesized by pulsed laser ablation: Size distributions and nanoscale structure," *Applied Surface Science* **129**, 355–361 (1998).
- ⁸A. P. Caricato, M. Fernández, M. Ferrari, G. Leggieri, M. Martino, M. Mattarelli, M. Montagna, V. Resta, L. Zampedri, R. M. Almeida, M. C. Gonçalves, L. Fortes, and L. F. Santos, "Er³⁺-doped tellurite waveguides deposited by excimer laser ablation," *Materials Science and Engineering B: Solid-State Materials for Advanced Technology* **105**, 65–69 (2003).
- ⁹M. Bouazaoui, B. Capoen, P. Caricato, A. P. Chiasera, A. Fazzi, M. Ferrari, G. Leggieri, M. Martino, M. Mattarelli, M. Montagna, F. Romano, T. Tunno, S. Turrel, and K. Vishnubhatla, "Pulsed laser deposition of Er doped tellurite films on large area," *Journal of Physics: Conference Series* **59**, 475–478 (2007).
- ¹⁰M. Martino, A. P. Caricato, M. Fernández, G. Leggieri, A. Jha, M. Ferrari, and M. Mattarelli, "Pulsed laser deposition of active waveguides," *Thin Solid Films* **433**, 39–44 (2003).
- ¹¹R. K. Singh, D. Bhattacharya, and J. Narayan, "Subsurface heating effects during pulsed laser evaporation of materials," *Applied Physics Letters* **57**, 2022–2024 (1990).
- ¹²E. G. Gamaly, A. V. Rode, and B. Luther-Davies, "Film deposition," *Pulsed laser deposition of thin films: applications-led growth of functional materials* (2007), 99.
- ¹³C. Boulmer-Leborgne, R. Benzerga, D. Scuderi, J. Perrière, O. Albert, J. Etchepare, and E. Millon, "Femtosecond laser beam in interaction with materials for thin film deposition," Proceedings of SPIE - The International Society for Optical Engineering **6261 II**, 2–10 (2006).
- ¹⁴J. Perrière, C. Boulmer-Leborgne, R. Benzerga, and S. Tricot, "Nanoparticle formation by femtosecond laser ablation," *Journal of Physics D: Applied Physics* **40**, 7069–7076 (2007).
- ¹⁵B. Rethfeld, D. S. Ivanov, M. E. Garcia, and S. I. Anisimov, "Modelling ultrafast laser ablation," *Journal of Physics D: Applied Physics* **50**, 193001 (2017).
- ¹⁶S. Amoroso, R. Bruzzese, N. Spinelli, R. Velotta, M. Vitiello, X. Wang, G. Ausanio, V. Iannotti, and L. Lanotte, "Generation of silicon nanoparticles via femtosecond laser ablation in vacuum," *Applied Physics Letters* **84**, 4502–4504 (2004).
- ¹⁷P. Balling and J. Schou, "Femtosecond-laser ablation dynamics of dielectrics: Basics and applications for thin films," *Reports on Progress in Physics* **76**, 036502 (2013).
- ¹⁸M. Sanz, M. Loopez-Arias, J. F. Marco, R. de Nalda, S. Amoroso, G. Ausanio, S. Lettieri, R. Bruzzese, X. Wang, and M. Castillejo, "Ultrafast laser ablation and deposition of wide band gap semiconductors," *The Journal of Physical Chemistry C* **115**, 3203–3211 (2011).
- ¹⁹E. Kumi-Barimah, M. W. Ziarko, N. Bamiedakis, I. H. White, R. V. Penty, and G. Jose, "Erbium-doped glass nanoparticle embedded polymer thin films using femtosecond pulsed laser deposition," *Optical Materials Express* **8**, 1997–2007 (2018).
- ²⁰J. Chandrappan, M. Murray, T. Kakkar, P. Petrik, E. Agocs, Z. Zolnai, D. P. Steenson, A. Jha, and G. Jose, "Target dependent femtosecond laser plasma implantation dynamics in enabling silica for high density erbium doping," *Scientific Reports* **5**, 14037 (2015).
- ²¹S. A. Kamil, J. Chandrappan, M. Murray, P. Steenson, T. F. Krauss, and G. Jose, "Ultrafast laser plasma doping of Er³⁺ ions in silica-on-silicon for optical waveguiding applications," *Optics Letters* **41**, 4684 (2016).
- ²²B. D. O. Richards, A. Boontan, T. Mann, E. Kumi Barimah, C. Russell, D. P. Steenson, and G. Jose, "Tm³⁺ tellurite-modified-silica glass thin films fabricated using ultrafast laser plasma doping," *IEEE Journal of Selected Topics in Quantum Electronics* **25**, 1–8 (2019).
- ²³J. Chandrappan, M. Murray, P. Petrik, E. Agocs, Z. Zolnai, A. Tempez, S. Legendre, D. P. Steenson, A. Jha, and G. Jose, "Doping silica beyond limits with laser plasma for active photonic materials," *Optical Materials Express* **5**, 2849 (2015).
- ²⁴T. Mann, R. Mathieson, M. Murray, B. Richards, and G. Jose, "Femtosecond laser ablation properties of Er³⁺ ion doped zinc-sodium tellurite glass," *Journal of Applied Physics* **124**, 044903 (2018).
- ²⁵G. Franzò, F. Priolo, and S. Coffa, "Understanding and control of the erbium non-radiative de-excitation processes in silicon," *Journal of Luminescence* **80**, 19–28 (1998).
- ²⁶N. Hamelin, P. G. Kik, J. F. Suyver, K. Kikoin, A. Polman, A. Schöneckner, and F. W. Saris, "Energy backtransfer and infrared photoresponse in erbium-doped silicon p-n diodes," *Journal of Applied Physics* **88**, 5381–5387 (2000).
- ²⁷A. Kenyon, "Recent developments in rare-earth doped materials for optoelectronics," *Progress in Quantum Electronics* **26**, 225–284 (2002).
- ²⁸C. Creatore, L. C. Andreani, M. Miritello, R. Lo Savio, and F. Priolo, "Modification of erbium radiative lifetime in planar silicon slot waveguides," *Applied Physics Letters* **94**, 103112 (2009).
- ²⁹J. Schindelin, I. Arganda-Carreras, E. Frise, V. Kaynig, M. Longair, T. Pietzsch, S. Preibisch, C. Rueden, S. Saalfeld, B. Schmid, and others, "Fiji: An open-source platform for biological-image analysis," *Nature methods* **9**, 676 (2012).
- ³⁰C. A. Schneider, W. S. Rasband, and K. W. Eliceiri, "NIH image to imageJ: 25 years of image analysis," *Nature Methods* **9**, 671 (2012).
- ³¹D. Nečas and P. Klapetek, Gwyddion (2018).
- ³²D. Nečas and P. Klapetek, "Gwyddion: An open-source software for SPM data analysis," *Open Physics* **10**, 181–188 (2012).
- ³³The spectral shift becomes more significant in GXID as the shallower angle results in a longer path length through the crystal planes.
- ³⁴B. Fultz and J. M. Howe, *Transmission electron microscopy and diffractometry of materials* (Springer Science & Business Media, 2012).
- ³⁵J. Chandrappan, "Femtosecond laser plasma assisted rare-earth doping in silica for integrated optics," Ph.D. thesis, University of Leeds (2015).
- ³⁶S. A. Kamil, "Ultrafast laser plasma doping of rare earth ions for optical waveguiding applications," Ph.D. thesis, University of Leeds (2018).
- ³⁷J. Chandrappan, V. Khetan, M. Ward, M. Murray, and G. Jose, "Devitrification of ultrafast laser plasma produced metastable glass layer," *Scripta Materialia* **131**, 37–41 (2017).
- ³⁸L. Le Neindre, S. Jiang, B.-C. Hwang, T. Luo, J. Watson, and N. Peyghambarian, "Effect of relative alkali content on absorption linewidth in erbium-doped tellurite glasses," *Journal of Non-Crystalline Solids* **255**, 97–102 (1999).
- ³⁹S. Manning, H. Ebendorff-Heidepriem, and T. M. Monro, "Ternary tellurite glasses for the fabrication of nonlinear optical fibres," *Optical Materials Express* **2**, 140 (2012).
- ⁴⁰S. Amoroso, G. Ausanio, R. Bruzzese, M. Vitiello, and X. Wang, "Femtosecond laser pulse irradiation of solid targets as a general route to nanoparticle formation in a vacuum," *Physical Review B - Condensed Matter and Materials Physics* **71**, 033406 (2005).
- ⁴¹S. Amoroso, R. Bruzzese, N. Spinelli, R. Velotta, M. Vitiello, and X. Wang, "Emission of nanoparticles during ultrashort laser irradiation of silicon targets," *Europhysics Letters (EPL)* **67**, 404–410 (2004).
- ⁴²A. Ben-Yakar and R. L. Byer, "Femtosecond laser ablation properties of borosilicate glass," *Journal of Applied Physics* **96**, 5316–5323 (2004).
- ⁴³P. K. Diwakar, S. S. Harilal, M. C. Phillips, and A. Hassanein, "Characterization of ultrafast laser-ablation plasma plumes at various Ar ambient pressures," *Journal of Applied Physics* **118**, 043305 (2015).
- ⁴⁴E. G. Gamaly, B. Luther-Davies, V. Z. Kolev, N. R. Madsen, M. Duering, and A. V. Rode, "Ablation of metals with picosecond laser pulses: Evidence of long-lived non-equilibrium surface states," *Laser and Particle Beams* **23**, 167–176 (2005).
- ⁴⁵A. Polman, "Erbium implanted thin film photonic materials," *Journal of Applied Physics* **82**, 1–39 (1997).

- ⁴⁶P. K. Diwakar, S. S. Harilal, A. Hassanein, and M. C. Phillips, "Expansion dynamics of ultrafast laser produced plasmas in the presence of ambient argon," *Journal of Applied Physics* **116**, 133301 (2014).
- ⁴⁷R. J. Glauber and M. Lewenstein, "Quantum optics of dielectric media," *Physical Review A* **43**, 467–491 (1991).
- ⁴⁸W. Żakowicz and M. Janowicz, "Spontaneous emission in the presence of a dielectric cylinder," *Physical Review A - Atomic, Molecular, and Optical Physics* **62**, 013820 (2000).
- ⁴⁹H. Khosravi and R. Loudon, "Vacuum field fluctuations and spontaneous emission in the vicinity of a dielectric surface," *Proc. R. Soc. Lond. A* **433**, 337–352 (1991).
- ⁵⁰C. Creatore and L. C. Andreani, "Quantum theory of spontaneous emission in multilayer dielectric structures," *Physical Review A* **78**, 063825 (2008).
- ⁵¹E. Snoeks, A. Lagendijk, and A. Polman, "Measuring and modifying the spontaneous emission rate of erbium near an interface," *Physical Review Letters* **74**, 2459 (1995).
- ⁵²W. Miniscalco, "Optical and electronic properties of rare earth ions in glasses," in *Rare earth doped fiber lasers and amplifiers* (Marcel Dekker, Inc., 1993), Chap. 2.
- ⁵³L. Zampedri, M. Mattarelli, M. Montagna, and R. Gonçalves, "Evaluation of local field effect on the 4I13/2 lifetimes in Er-doped silica-hafnia planar waveguides," *Physical Review B* **75**, 073105 (2007).
- ⁵⁴E. Snoeks, P. G. Kik, and A. Polman, "Concentration quenching in erbium implanted alkali silicate glasses," *Optical Materials* **5**, 159–167 (1996).
- ⁵⁵G. M. Miller, R. M. Briggs, and H. A. Atwater, "Achieving optical gain in waveguide-confined nanocluster-sensitized erbium by pulsed excitation," *Journal of Applied Physics* **108**, 063109 (2010).